IET Energy Systems Integration

WILEY

天津大学 Tianjin University | IET The Institution of Engineering and Technology

ORIGINAL RESEARCH OPEN ACCESS

High-Power Voltage Source Converter for Integration of Battery in Power System

Subir Karmakar[1] | Bhim Singh[1] | Ambrish Chandra[2] | Kamal Al-Haddad[2]

[1]Department of Electrical Engineering, Indian Institute of Technology Delhi, New Delhi, India | [2]Department of Electrical Engineering, Ecole de Technology Superieure, Montréal, Canada

Correspondence: Subir Karmakar (subir.iitd@gmail.com)

Received: 26 August 2024 | **Revised:** 3 May 2025 | **Accepted:** 15 May 2025

Funding: This work was supported by the ANRF Government of India for funding this work under ANRF NSC Fellowship: UKICERI: RP03391, UI-ASSIST: RP03443, and DST: RP03357 (FIST scheme).

Keywords: battery storage plants | power convertors | power electronics | power system harmonics | renewable energy sources

ABSTRACT

To address grid instability caused by intermittent renewable energy, this work proposes utility-scale battery energy storage (BES) integration using a hybrid multilevel and multipulse voltage source converter (VSC) topology, which overcomes the limitations of conventional converters in efficiency, scalability and harmonic performance for high-power, high-voltage applications. VSC employs 13-level H-bridge converters and 30-pulse high voltage converters to mitigate voltage harmonics. By combining multipulse technique with selective harmonics elimination, low total harmonic distortion is achieved for VSC output voltage and grid currents. Utilising multiple cascaded H-bridge (CHB) converters and transformers increases VSC power and energy capacity for BES plant to deliver energy at a 400-kV voltage level to grid. A 1000-MW VSC with a 6000-MWh BES plant is simulated in MATLAB and implemented on a real-time platform to study its steady-state, harmonics and dynamic performances.

1 | Introduction

The growing adoption of clean energy is essential for combating climate change and ensuring energy security [1]. Solar and wind power deployment has surged and is expected to continue rising. However, the high penetration of these sources presents challenges for grid stability. At peak production, supply can exceed demand, raising grid frequency. To maintain stability, curtailment or reducing conventional generation (thermal and hydro) is often required. Additionally, their output is weather-dependent, fluctuating due to cloud cover, rain and wind variations, affecting voltage and frequency stability [2, 3].

Addressing these issues requires innovative solutions. Large-scale battery energy storage (BES) is a key strategy for stabilising the grid. BES stores surplus energy during peak generation, reducing curtailment and optimising existing assets. This improves efficiency, lowers operational costs and minimises reliance on conventional power plants. During peak demand or low generation periods, BES discharges stored energy, ensuring a stable and uninterrupted supply. This strengthens grid reliability, providing consistent energy even during disruptions [4–6].

In addition to storing surplus energy, BES systems play a pivotal role in providing diverse grid ancillary services essential for maintaining grid stability and reliability. One critical application is grid voltage regulation, where BES systems can supply or absorb reactive power to ensure voltage levels remain within specified limits, thereby supporting the power quality and reducing stress on conventional grid equipment. Furthermore, BES systems significantly contribute to grid frequency control

by responding rapidly to frequency deviations. They can inject active power during under-frequency events or absorb excess power during over-frequency conditions, helping to maintain the system's frequency stability. Beyond these services, BES systems enable load shifting, where energy stored during periods of low demand is dispatched during peak demand periods. They also support black start capability, allowing grid restoration after a blackout without relying on traditional synchronous generators.

The demand for BES systems is surging exponentially, both in terms of energy storage capacity (MWh) and power rating (MW), particularly for large-scale grid applications. BES systems are increasingly deployed at the substation level, where they can enhance grid reliability and stability by efficiently managing energy flows and addressing fluctuations in supply and demand. By strategically situating BES plants at substations, they can optimise grid operations. This placement enables BES systems to act as a critical buffer, ensuring a more stable and reliable grid, even amidst fluctuating power requirements or unanticipated disturbances in the energy network. However, establishment of such a sizeable BES system requires high-capacity power converters. These converters serve as linchpins that enable seamless integration of large-scale BES systems into the grid. Multilevel [7–11] and multipulse [12–15] converters are traditionally used for high-capacity power converter applications such as high-voltage DC transmission (HVDC), medium-voltage drives, e-mobility, static compensators (STATCOM) or power flow controllers (PFC), e-mobility and aircraft power system.

The scalability of the presented BES system for large-scale grid applications is achieved through modularity, and BES units are typically designed with a modular architecture, allowing for incremental additions of battery modules, inverters and associated infrastructures. This modular approach enables utilities to start with smaller systems and expand them as demand increases, optimising capital expenditure and reducing upfront costs. Each module can operate independently or in conjunction with others, ensuring smooth scalability without disrupting existing operations.

The economic feasibility of BES in large-scale grid applications depends on costs, revenue streams and overall system value. The decreasing cost trends of batteries, especially lithium-ion, driven by economies of scale and technological advancements, make large-scale applications more economically viable. BES revenue generation can be maximised by leveraging its diverse applications. BES revenue can be maximised through ancillary services like frequency regulation, voltage support and load shifting. It enables energy arbitrage by storing low-cost off-peak electricity for sale during peak demand, leveraging dynamic pricing. Additionally, BES defers costly grid upgrades, creating savings and revenue-sharing opportunities with utilities, enhancing financial returns.

Li et al. [1] have presented the use of BES for integrating renewable energy into power systems, addressing reliability issues related to thermally induced degradation and thermal runaway (TR) effects. Guo et al. [2] have presented reviews of optimisation methods for energy storage management to handle renewable energy volatility, categorising them into multistage, online and multi-timescale optimisations to aid in integrating renewable energy into power grids. Elsaied et al. [3] have focused on integrating renewable sources and energy storage devices to enhance the stability of a three-area system. Suthar et al. [4] have developed an energy management platform for battery-based energy storage and solar PV systems. It features an optimal scheduling algorithm for BES to cut energy costs and a fuzzy logic control strategy for aeration blowers to boost efficiency. Bera et al. [6] have emphasised the using energy storage systems (ESSs) to provide virtual inertia and stabilise grid frequency amid increasing renewable energy integration. It develops an analytical approach to size ESSs based on probabilistic models of conventional and renewable generation. Scaglione et al. [7] in their work, have used a three-phase five-level cascaded H-bridge multilevel inverter (CHBMI) in a permanent magnet synchronous machine drive. X. Wang et al. [8] have suggested a three-phase cascaded H-bridge inverter, detailing a fault-tolerant control method using redundant voltage vectors to handle switch faults. It introduces novel power balancing strategies to mitigate output power imbalances. Mohammadhassani and Mehrizi-Sani [9] have proposed a fault-tolerant model predictive control (FT SHE-MPC) for modular multilevel converters (MMCs) using selective harmonic elimination (SHE). The approach maintains harmonic performance and manages switch failures, resulting in faster fault recovery and lower capacitor ripple. Kala et al. [10] have presented a hybrid approach using Grey Wolf optimisation (GWO) and Newton–Raphson (NR) methods for solving the selective harmonic elimination (SHE) problem in adaptive DC bus multilevel inverters (MLIs). It achieves efficient harmonic control and dynamic operation in photovoltaic (PV) systems. Pan et al. [11] have presented a unified switching frequency minimised harmonic mitigation (SFMHM) model for asymmetric cascaded H-bridge (ACHB) converters, focusing on optimising switching patterns to minimise switching frequency while achieving selective harmonic elimination (SHE) and mitigation of low-order harmonics. Abdollahi and Gharehpetian [12] have compared passive harmonic reduction circuits (PHRCs) for multipulse rectifiers (MPRs) by standardising source and load conditions. It assesses PHRCs on operation, size, losses, THD, complexity, reliability and cost to recommend the best options for MPRs in industrial applications. Lian et al. [13] have compared traditional and unconventional interphase reactors (IPRs) in a 36-pulse diode rectifier. It evaluates how each IPR affects operation modes, currents and voltages, finding both reduce input line current distortion to 5%. Q. Li, Meng et al. [14] have presented a 30-pulse converter employing passive voltage harmonic injection at the DC link. By injecting a square wave voltage at six times the supply frequency, it increases converter steps from 18 to 30, effectively reducing input voltage harmonics. J. Wang et al. [15] have introduced a 24-pulse star converter utilising two pulse-doubling interphase reactors (PD-IPRs), which increase the converter's pulse count from 6 to 24. It achieves near-sinusoidal input line currents with low total harmonic distortion, employing a straightforward and cost-effective design. Zhang et al. [16] have employed d-q vector control in the voltage source converter control approach.

In this study, a VSC configuration is presented to enhance the capacity of BES plant. The battery connection uses a straight hanging arrangement [5] with a 13-level CHB in order to attain

high voltage and power at the CHB output. A multipulse (30-pulse) step-up transformer is coupled with five 13-level CHBs in a VSC configuration. This transformer operates at line frequency and is crucial to meet grid code requirements. It eliminates DC injection into the grid, provides magnetic isolation from the grid and facilitates efficient bulk power evacuation by stepping up the VSC or plant voltage to high voltage or extra high voltage levels.

2 | BES Plant Architecture and Control Strategy

BES plant configuration with 1000 MW capacity is depicted in Figure 1. It consists of 132 kV 13-level CHBs with 30-pulse converter transformer-based VSC of rating 50 MW. Twenty such VSCs are directly connected to 132 kV bus, with each bus handling five VSCs totalling 250 MW. To achieve 1000 MW capacity, four 132 kV buses are utilised, each linked to a 400-kV/132-kV step-up transformer rated at 500 MVA. A 400-kV bus is connected to two 500 MVA transformers, enabling two outgoing and two incoming feeders, along with a bus coupler. Power evacuation is managed via two 400 kV outgoing feeders. Each VSC unit integrates 50 MW/300 MWh, a six-hour lithium-ion battery storage system.

2.1 | VSC Configuration

This presented structure of a VSC, shown in Figure 2, incorporates 30-pulse converter transformers with five 13-level CHB converters. Each 13-level CHB is equipped with 18 H-bridge cells. Each phase incorporates series of connected six H-bridge cells to augment voltage. The DC input side of each H-bridge cell is linked to a series-parallel arrangement of lithium-ion battery modules. A 30-pulse converter transformer low-voltage (LV) side is connected to a set of 13-level CHBs. These CHBs are configured with five LV windings, each phase-shifted differently. On the LV side, the transformer incorporates one delta winding and four polygon windings. These windings facilitate the generation of a 132-kV output voltage from high-voltage (HV) side, which is then connected to a 132-kV bus. Figure 3 illustrates the configuration and switching states of H-bridge cells. In Figure 4, the phase voltage waveform of the 13-level CHB converter is shown, highlighting H-bridge cells switching states.

LV windings are phase-shifted for 30-pulse converter operation: polygon windings T1 at +24°, T2 at +12°, delta winding T3 at 0°

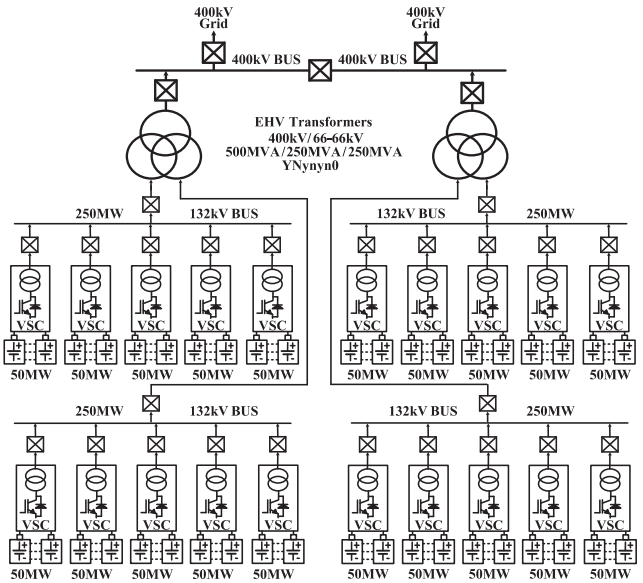

FIGURE 1 | Configuration of BES plant.

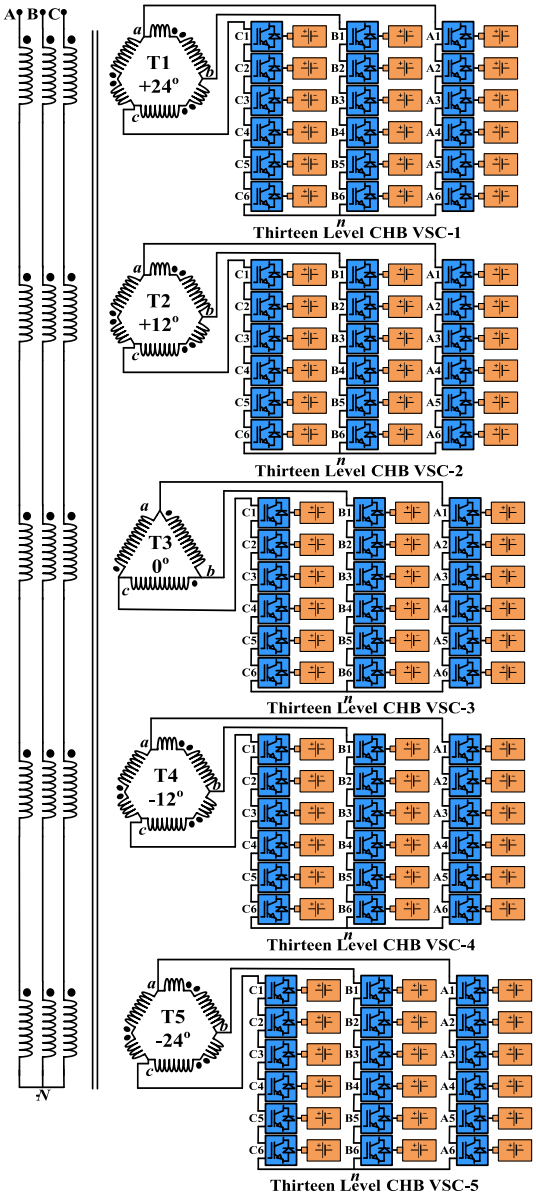

FIGURE 2 | Configuration of VSC.

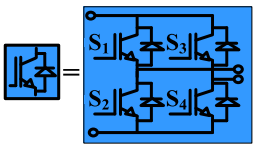

Switching States	S_1	S_2	S_3	S_4
O	1	0	1	0
P	1	0	0	1
O	0	1	0	1
N	0	1	1	0

FIGURE 3 | Switching states and configurations of an H-bridge cell.

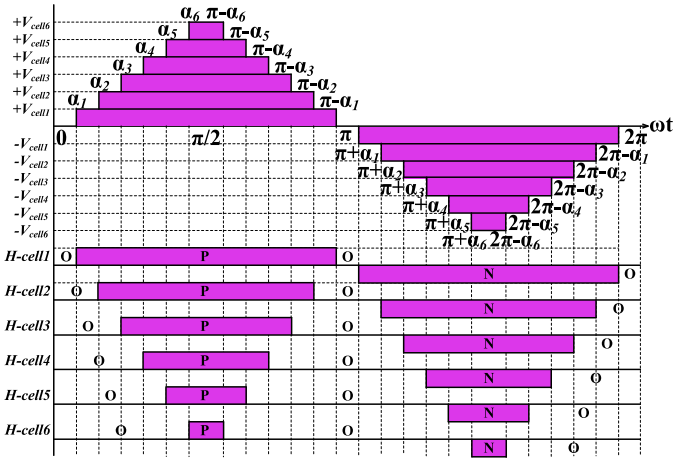

FIGURE 4 | Switching states and phase voltage of CHB.

and polygon windings T4 at −12° and T5 at −24°. This configuration allows VSC to operate with 30- pulses, effectively eliminates harmonics of order 5th (h_5), 7th (h_7), 11th (h_{11}), 13th (h_{13}), 17th (h_{17}), 19th (h_{19}), 23rd (h_{23}), 25th (h_{25}), 35th (h_{35}), 37th (h_{37}), 41st (h_{41}), 43rd (h_{43}), 47th (h_{47}), 49th (h_{49}), 53rd (h_{53}), 55th (h_{55}), 65th (h_{65}), 67th (h_{67}), 71st (h_{71}), 73rd (h_{73}), 77th (h_{77}), 79th (h_{79}), 83rd (h_{83}), 85th (h_{85}), 95th (h_{95}) and 97th (h_{97}).

Fundamental SHE techniques [9–11] are employed to eliminate the remaining harmonics from output voltages of VSC. Harmonics up to 100th order, including 29th (h_{29}), 31st (h_{31}), 59th (h_{59}), 61st (h_{61}), 89th (h_{89}) and 91st (h_{91}), are effectively mitigated through this approach. Six distinct switching angles, represented as ($\alpha_1, \alpha_2, \alpha_3, \alpha_4, \alpha_5, and\ \alpha_6$), are utilised to control the H-bridge cells' switching operations.

13-level CHB H-bridge cells AC line voltages are defined as

$$v_{\text{cell1}}(t) = \sum_{n=1,3,5,\ldots}^{\infty} \frac{4\sqrt{3}V_{cell1}}{n\pi}\cos(n\alpha_1)\sin(n\omega t) \tag{1}$$

$$v_{\text{cell2}}(t) = \sum_{n=1,3,5,\ldots}^{\infty} \frac{4\sqrt{3}V_{cell2}}{n\pi}\cos(n\alpha_2)\sin(n\omega t) \tag{2}$$

$$v_{\text{cell3}}(t) = \sum_{n=1,3,5,\ldots}^{\infty} \frac{4\sqrt{3}V_{cell3}}{n\pi}\cos(n\alpha_3)\sin(n\omega t) \tag{3}$$

$$v_{\text{cell4}}(t) = \sum_{n=1,3,5,\ldots}^{\infty} \frac{4\sqrt{3}V_{cell4}}{n\pi}\cos(n\alpha_4)\sin(n\omega t) \tag{4}$$

$$v_{\text{cell5}}(t) = \sum_{n=1,3,5,\ldots}^{\infty} \frac{4\sqrt{3}V_{cell5}}{n\pi}\cos(n\alpha_5)\sin(n\omega t) \tag{5}$$

$$v_{\text{cell6}}(t) = \sum_{n=1,3,5,\ldots}^{\infty} \frac{4\sqrt{3}V_{cell6}}{n\pi}\cos(n\alpha_6)\sin(n\omega t) \tag{6}$$

Considering,

$$V_{\text{cell}} = V_{\text{cell1}} = V_{\text{cell2}} = V_{\text{cell3}} = V_{\text{cell4}} = V_{\text{cell5}} = V_{\text{cell6}} \tag{7}$$

Hence, 13-level CHB line voltage is defined as

$$v(t) = v_{\text{cell1}}(t) + v_{\text{cell2}}(t) + v_{\text{cell3}}(t) + v_{\text{cell4}}(t) + v_{\text{cell5}}(t) + v_{\text{cell6}}(t) \tag{8}$$

$$v(t) = \sum_{n=1,3,5,\ldots}^{\infty} \frac{4\sqrt{3}V_{cell}}{n\pi}\left[\cos(n\alpha_1) + \cos(n\alpha_2) + \cos(n\alpha_3) + \cos(n\alpha_4) + \cos(n\alpha_5) + \cos(n\alpha_6)\right]\sin(n\omega t) \tag{9}$$

A 13-level CHB fundamental line voltage is defined as

$$v(t) = \frac{4\sqrt{3}V_{cell}}{\pi}\left[\cos(\alpha_1) + \cos(\alpha_2) + \cos(\alpha_3) + \cos(\alpha_4) + \cos(\alpha_5) + \cos(\alpha_6)\right]\sin(\omega t) \tag{10}$$

Hence,

$$v(t) = V\sin(\omega t) \tag{11}$$

Where, peak voltage V is defined as

$$V = \frac{4\sqrt{3}V_{cell}}{\pi}\left[\cos(\alpha_1) + \cos(\alpha_2) + \cos(\alpha_3) + \cos(\alpha_4) + \cos(\alpha_5) + \cos(\alpha_6)\right] \tag{12}$$

A 13-level CHB modulation index is defined as

$$M = \frac{\pi V}{4\sqrt{3}SV_{cell}} \tag{13}$$

Where $S = 6$, per phase series connected H-bridge cell number.

Figure 5 illustrates the winding connections of a star-polygon transformer, which features both positive and negative phase shifts. Voltages for long winding (V_{nL}) and short winding (V_{nS}) are expressed in terms of line voltage (V_{LS}) as follows:

$$V_{nL} = \left(\frac{2}{\sqrt{3}}\right)V_{LS}\sin(60^o - \theta) = k_1 V_{LS} \tag{14}$$

$$V_{nS} = \left(\frac{2}{\sqrt{3}}\right)V_{LS}\sin(\theta) = k_2 V_{LS} \tag{15}$$

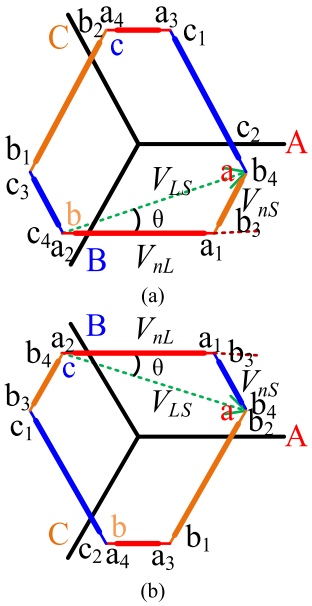

FIGURE 5 | Star/polygon connection: (a) positive phase, (b) negative phase.

The calculated values of constants k_1 and k_2 are tabulated in Table 1.

T1 transformer secondary windings line voltages are defined as

$$\left.\begin{aligned} v_{ab1}(t) &= V\sin(\omega t + 24^o) \\ v_{bc1}(t) &= V\sin(\omega t - 120^o + 24^o) \\ v_{ca1}(t) &= V\sin(\omega t + 120^o + 24^o) \end{aligned}\right\} \tag{16}$$

T2 transformer secondary windings line voltages are defined as

$$\left.\begin{aligned} v_{ab2}(t) &= V\sin(\omega t + 12^o) \\ v_{bc2}(t) &= V\sin(\omega t - 120^o + 12^o) \\ v_{ca2}(t) &= V\sin(\omega t + 120^o + 12^o) \end{aligned}\right\} \tag{17}$$

T3 transformer secondary windings line voltages are defined as

$$\left.\begin{aligned} v_{ab3}(t) &= V\sin(\omega t) \\ v_{bc3}(t) &= V\sin(\omega t - 120^o) \\ v_{ca3}(t) &= V\sin(\omega t + 120^o) \end{aligned}\right\} \tag{18}$$

T4 transformer secondary windings line voltages are defined as

TABLE 1 | Calculation of k_1 and k_2.

Phase shift angle (θ)	k_1	k_2
24^o	$k_{11} = 0.6787$	$k_{12} = 0.4697$
12^o	$k_{21} = 0.8581$	$k_{22} = 0.2401$
-24^o	$k_{11} = 0.6787$	$k_{12} = 0.4697$
-12^o	$k_{21} = 0.8581$	$k_{22} = 0.2401$

$$\left.\begin{aligned} v_{ab4}(t) &= V\sin(\omega t - 12^o) \\ v_{bc4}(t) &= V\sin(\omega t - 120^o - 12^o) \\ v_{ca4}(t) &= V\sin(\omega t + 120^o - 12^o) \end{aligned}\right\} \tag{19}$$

T5 transformer secondary windings line voltages are defined as

$$\left.\begin{aligned} v_{ab5}(t) &= V\sin(\omega t - 24^o) \\ v_{bc5}(t) &= V\sin(\omega t - 120^o - 24^o) \\ v_{ca5}(t) &= V\sin(\omega t + 120^o - 24^o) \end{aligned}\right\} \tag{20}$$

After referring the transformer secondary voltages as defined in Equations (16–20) to the primary side, the VSC HV side A-phase voltage (phase) is calculated as

$$v_{AN}(t) = mV\,C\sin(\omega t) \tag{21}$$

Where constant C is calculated as

$$\begin{aligned} C = [&2k_{11}\cos(24^o) - 2k_{12}\cos(120^o + 24^o) + 2k_{21}\cos(12^o) \\ &-2k_{22}\cos(120^o + 12^o) + 1] = 5 \end{aligned} \tag{22}$$

The transformer turn ratio is defined as

$$m = \frac{\text{HV side phase voltage}}{\text{LV side line voltage}} \tag{23}$$

VSC HV side A-phase voltage (phase) is redefined as

$$v_{AN}(t) = \frac{120\sqrt{3}mMV_{\text{cell}}}{\pi}\sin(\omega t) \tag{24}$$

VSC HV side line voltage is redefined as

$$v_{AB}(t) = \frac{120\sqrt{9}mMV_{\text{cell}}}{\pi}\sin(\omega t) \tag{25}$$

As per Equation (25), it is possible to regulate VSC voltage by controlling the 13-level CHBs modulation index (M) as shown in Equation (26).

$$\left.\begin{aligned} M &= \frac{1}{6}[\cos(\alpha_1) + \cos(\alpha_2) + \cos(\alpha_3) + \cos(\alpha_4) + \cos(\alpha_5) + \cos(\alpha_6)] \\ h_{29} &= \cos(29\alpha_1) + \cos(29\alpha_2) + \cos(29\alpha_3) + \cos(29\alpha_4) + \cos(29\alpha_5) + \cos(29\alpha_6) \\ h_{31} &= \cos(31\alpha_1) + \cos(31\alpha_2) + \cos(31\alpha_3) + \cos(31\alpha_4) + \cos(31\alpha_5) + \cos(31\alpha_6) \\ h_{59} &= \cos(59\alpha_1) + \cos(59\alpha_2) + \cos(59\alpha_3) + \cos(59\alpha_4) + \cos(59\alpha_5) + \cos(59\alpha_6) \\ h_{61} &= \cos(61\alpha_1) + \cos(61\alpha_2) + \cos(61\alpha_3) + \cos(61\alpha_4) + \cos(61\alpha_5) + \cos(61\alpha_6) \\ h_{95} &= \cos(95\alpha_1) + \cos(95\alpha_2) + \cos(95\alpha_3) + \cos(95\alpha_4) + \cos(95\alpha_5) + \cos(95\alpha_6) \\ h_{97} &= \cos(97\alpha_1) + \cos(97\alpha_2) + \cos(97\alpha_3) + \cos(97\alpha_4) + \cos(97\alpha_5) + \cos(97\alpha_6) \end{aligned}\right\} \tag{26}$$

Switching angles ($\alpha_1, \alpha_2, \alpha_3, \alpha_4, \alpha_5, and\ \alpha_6$) for CHB converters are computed based on different modulation values, as defined in (26) according to the SHE concept. These calculations aim to eliminate targeted harmonics from VSC voltage output [9–11]. Table 2 displays computed CHB switching angles and corresponding harmonic amplitudes, showcasing the effectiveness of this approach in harmonics mitigation. The single-phase synchronous DQ-based [15] control approach is utilised in VSC for control of active and reactive power, as shown in Figure 6.

3 | Results and Discussion

In MATLAB, a simulation of a BES plant with a capacity of 1000 MW and 6000 MWh is developed and then implemented in OPAL-RT, and the validation of its performance under simulated and real-time operation results is done. The real-time setup used in this work is presented in Figure 7.

3.1 | Steady-State Response

VSC 30-pulse converter operation effectiveness is validated by selecting switching angle values of zero ($\alpha_1 = \alpha_2 = \alpha_3 = \alpha_4 = \alpha_5 = \alpha_6 = 0°$) for H-bridge cells of 13-level CHB. Figure 8a depicts the phase voltage of a 13-level CHB and the voltages across its H-bridges. Each H-bridge cell conducts for 180°, aligning with single 180° pulse conducted by CHB phase voltage. Figure 8b shows the voltage waveform of VSC and HV side voltages of phase-shifting transformers T1 to T5. VSC voltage displays a staircase shape, characteristic of its 30-pulse operation, where each level incrementally increases. Switching angle values for 13-level CHBs are selected based on calculated values shown in Table 2 to illustrate the collective impact of SHE modulation and 30-pulse converter operation. This approach aims to showcase how these configurations work together to optimise performance and reduce harmonics in the system. Figure 9a illustrates the phase voltage of a 13-level CHB converter and the voltages across its H-bridge cells, which is conducted based on selected switching angles, resulting in varying pulse widths and a staircase-shaped voltage with 13 levels. Figure 9b shows high-voltage side voltages of phase-shifting transformers T1 to T5 and VSC waveform. A collective operation of CHB SHE and 30-pulse converter produces a VSC output that is close to a pure sine wave, demonstrating harmonics reduction and high waveform quality. Figure 10 shows voltage of VSC and its associated harmonics, yielding a total harmonic distortion (THD) of 1.15%. The output currents waveform of the BES plant at the 400-kV voltage level is depicted in Figure 11a, and the BES plant's current THD under varying VSC power outputs is demonstrated in Figure 11b–d. The results indicate that the plant maintains a low current THD, ranging from 0.24% to 0.45%, with negligible harmonic contents up to the 100th order.

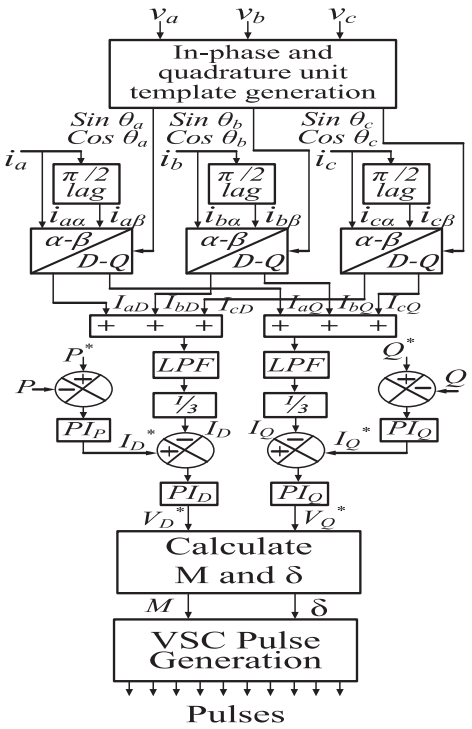

FIGURE 6 | VSC control strategy.

TABLE 2 | Calculated harmonics and switching angles of a 13-level CHB.

Modulation index (M)	1.0	0.95	0.9	0.85	0.8	0.75	0.7	0.65	0.6
Switching angles	$\alpha_1 = 00.00°$	$\alpha_1 = 01.67°$	$\alpha_1 = 02.24°$	$\alpha_1 = 00.47°$	$\alpha_1 = 00.00°$	$\alpha_1 = 08.85°$	$\alpha_1 = 05.62°$	$\alpha_1 = 06.46°$	$\alpha_1 = 35.03°$
	$\alpha_2 = 01.94°$	$\alpha_2 = 02.48°$	$\alpha_2 = 03.94°$	$\alpha_2 = 16.34°$	$\alpha_2 = 05.67°$	$\alpha_2 = 16.28°$	$\alpha_2 = 23.76°$	$\alpha_2 = 23.81°$	$\alpha_2 = 40.94°$
	$\alpha_3 = 02.02°$	$\alpha_3 = 05.94°$	$\alpha_3 = 19.63°$	$\alpha_3 = 21.95°$	$\alpha_3 = 33.63°$	$\alpha_3 = 37.56°$	$\alpha_3 = 39.53°$	$\alpha_3 = 56.67°$	$\alpha_3 = 49.62°$
	$\alpha_4 = 04.01°$	$\alpha_4 = 11.70°$	$\alpha_4 = 25.30°$	$\alpha_4 = 26.38°$	$\alpha_4 = 38.43°$	$\alpha_4 = 42.32°$	$\alpha_4 = 45.82°$	$\alpha_4 = 57.41°$	$\alpha_4 = 51.54°$
	$\alpha_5 = 05.92°$	$\alpha_5 = 28.04°$	$\alpha_5 = 35.14°$	$\alpha_5 = 43.55°$	$\alpha_5 = 51.97°$	$\alpha_5 = 58.64°$	$\alpha_5 = 56.61°$	$\alpha_5 = 62.41°$	$\alpha_5 = 66.99°$
	$\alpha_6 = 07.92°$	$\alpha_6 = 32.08°$	$\alpha_6 = 41.60°$	$\alpha_6 = 53.55°$	$\alpha_6 = 56.05°$	$\alpha_6 = 60.30°$	$\alpha_6 = 74.25°$	$\alpha_6 = 63.46°$	$\alpha_6 = 69.05°$
h_{29}	0.037	0.013	0.025	0.050	0.027	0.032	0.042	0.019	0.043
h_{31}	0.044	0.071	0.007	0.008	0.057	0.015	0.020	0.046	0.027
h_{59}	0.077	0.024	0.006	0.017	0.033	0.063	0.096	0.078	0.005
h_{61}	0.021	0.043	0.005	0.005	0.051	0.043	0.006	0.042	0.080
h_{89}	0.018	0.013	0.070	0.011	0.034	0.028	0.095	0.003	0.052
h_{91}	0.018	0.018	0.051	0.001	0.027	0.097	0.039	0.020	0.002

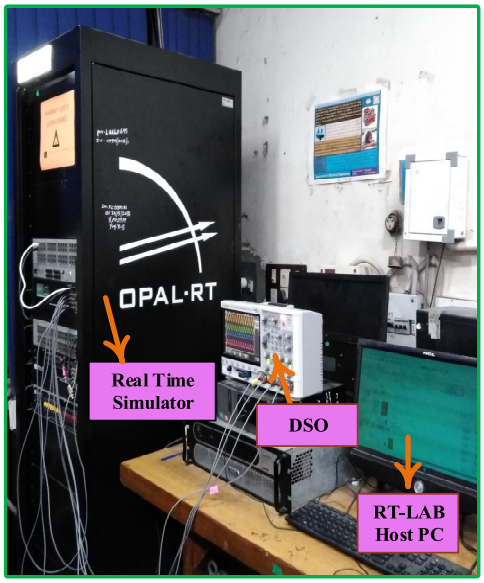

FIGURE 7 | Real-time setup.

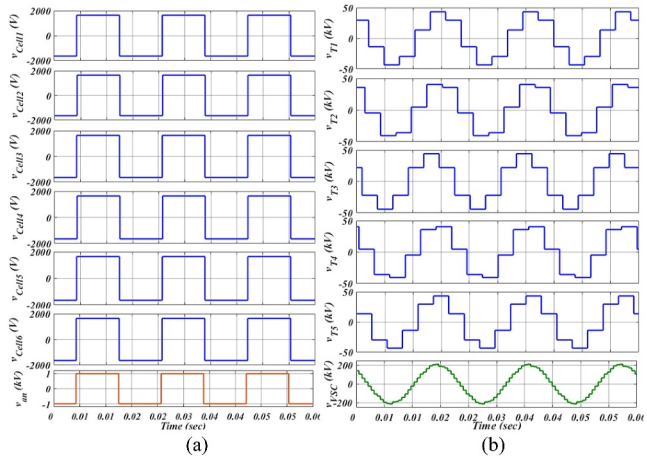

FIGURE 8 | Voltages CHB H-bridge cells and VSC using an equal switching angle (180°): (a) CHB H-bridge cells voltage and (b) transformers HV side voltage.

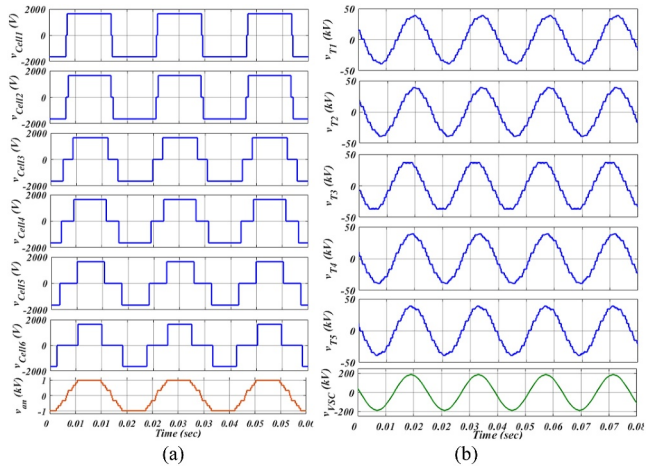

FIGURE 9 | Voltages of CHB H-bridge cells and VSC using SHE: (a) CHB H-bridge cells voltage and (b) transformers HV side voltage.

In Figure 12, the real-time waveform of VSC is depicted, demonstrating a THD of 1.119%. Figure 13 shows the real-time output current waveform of the BES plant at a 400-kV voltage level, with grid current achieving a THD of 0.238%.

3.2 | Dynamic Response

Figure 14 and Figure 15 show the BES plant's dynamic performance at different operational conditions. Figure 14a demonstrates the BES plant in a charging mode, where active power (P_{grid}) drawn from the grid increases from −500 MW to −1000 MW. As active power increases, the current drawn by the BES plant from the grid also rises, indicating an increased rate of energy storage. Figure 14b presents a similar scenario during the discharging phase. In this case, active power (P_{grid}) delivered to the grid increases from +500 MW to +1000 MW. This demonstrates the BES plant capability to supply higher amount of power back to the grid, with corresponding increase in current indicating energy being discharged. Figure 15 demonstrates the reactive power response of a BES plant. In Figure 15a, the BES plant is shown to consume reactive power from the grid, which is essential for maintaining voltage stability. Conversely, Figure 15b shows the BES plant delivering reactive power (Q_{grid}) to the grid. Throughout these operational changes, the current drawn by or supplied by the BES plant changes, accordingly, reflecting the dynamic response of the system to varying power demands. Figure 16 demonstrates the low voltage ride-through (LVRT) response of the BES during a sudden grid voltage dip from 100% to 30% of its nominal value. In this scenario, BES increases its reactive power injection into the grid and reactive power increases from 0 to 200MVAR. The active power output decreases from 1000 to 200 MW due to reduced terminal voltage and simultaneous rise in reactive power contribution. During this transient condition, the BES current remains nearly constant.

The reference active and reactive current contribution during the LVRT operation is calculated as

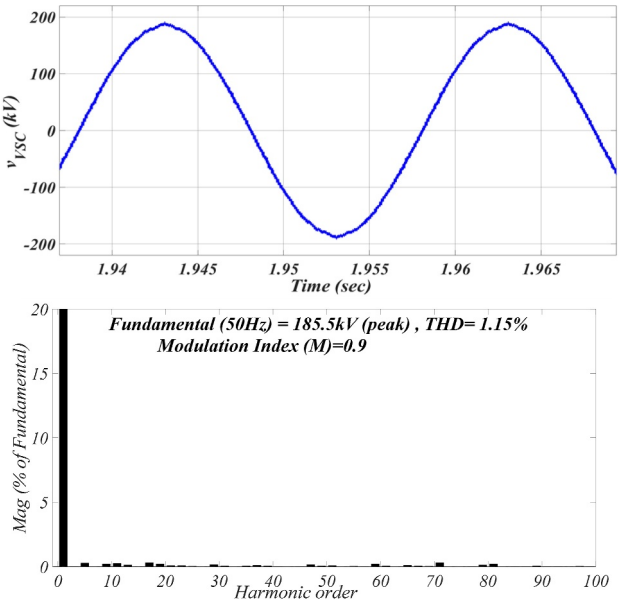

FIGURE 10 | Waveform and harmonics of VSC in the steady state.

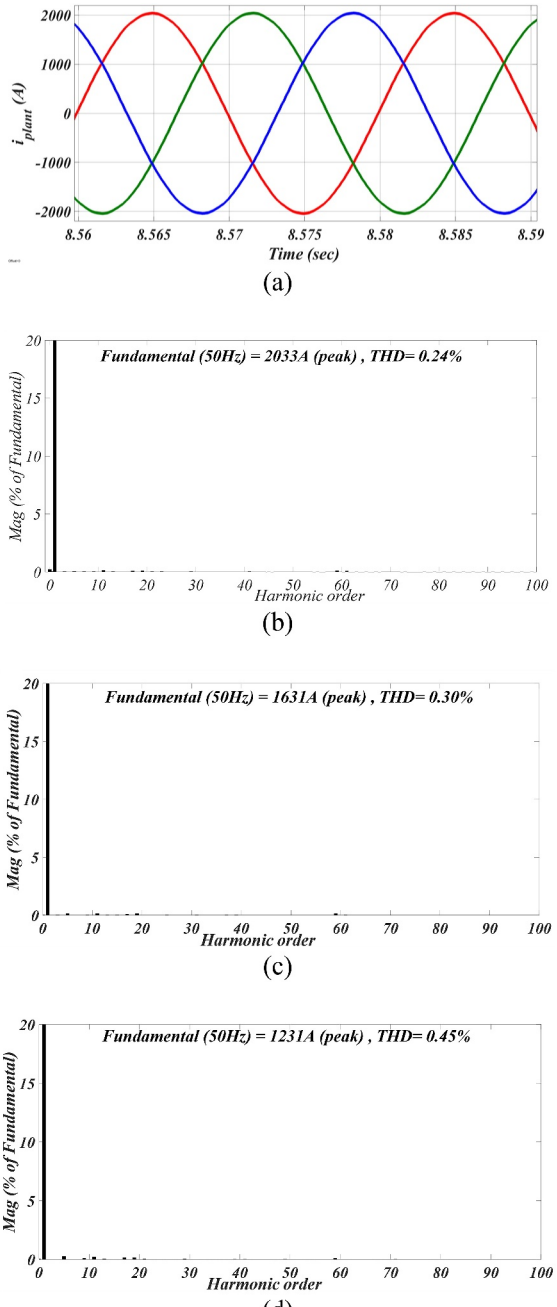

FIGURE 11 | BES plant current waveform (a) and harmonics with load variations, (b) 100% loading, (c) 80% loading, (d) 60% loading.

$$I_Q = k\,\Delta V * I_S,\ k = 1 \tag{27}$$

$$0 \le I_Q \le I_S \tag{28}$$

$$I_D = \sqrt{I_S{}^2 - I_Q{}^2} \tag{29}$$

Change in VSC terminal voltage is calculated as

$$\Delta V = V_n - V_{\text{drop}} \tag{30}$$

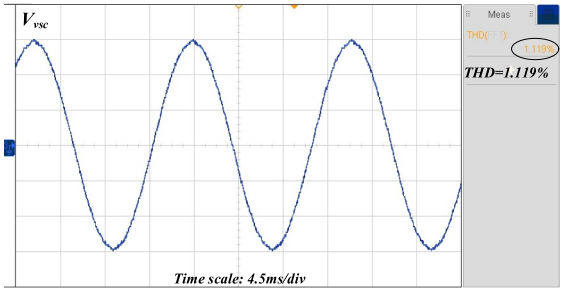

FIGURE 12 | Waveform and harmonics of VSC in the real-time steady state.

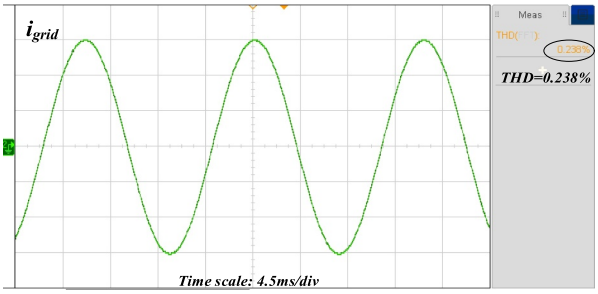

FIGURE 13 | BES plant real-time steady-state current waveform and harmonics.

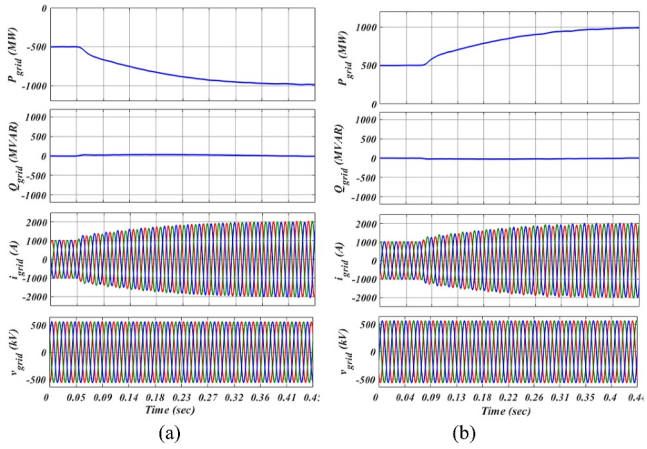

FIGURE 14 | Dynamic response of BES: (a) charging mode and (b) discharging mode.

where U_n and U_{drop} are the VSC terminal nominal voltage and voltage drop at the time of fault.

Considering this, the BES plant active and reactive power before and during LVRT with grid voltage drop to 30% of nominal voltage is calculated and shown in Table 3.

Figures 17–20 illustrate the real-time dynamic performance of the BES plant under various operational conditions. Figure 17 shows the BES plant in discharging mode, with active power (P_{grid}) delivered to the grid, increasing from +500 MW to +1000 MW, and a corresponding increase in current. Figure 18 depicts a decrease in active power (P_{grid}) from +1000 MW to +500 MW, indicating a reduction in energy discharge.

Figures 19–20 display the BES plant reactive power (Q_{grid}) response, with Figure 19 showing consumption from the grid and Figure 20 showing delivery to the grid. Throughout these changes, the current adjusts accordingly, reflecting the system's dynamic response to power demands.

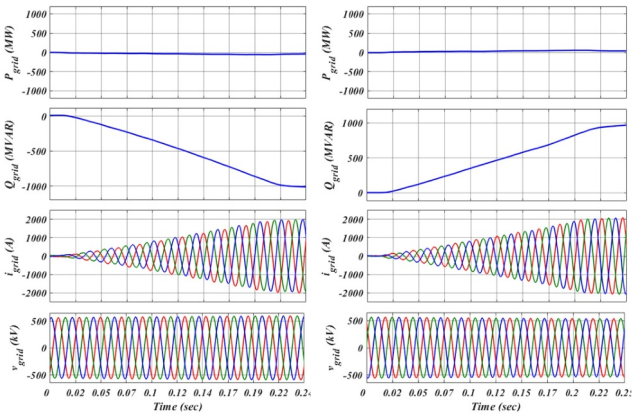

(a) (b)

FIGURE 15 | Reactive power dynamic response of the BES: (a) inductive operation and (b) capacitive operation.

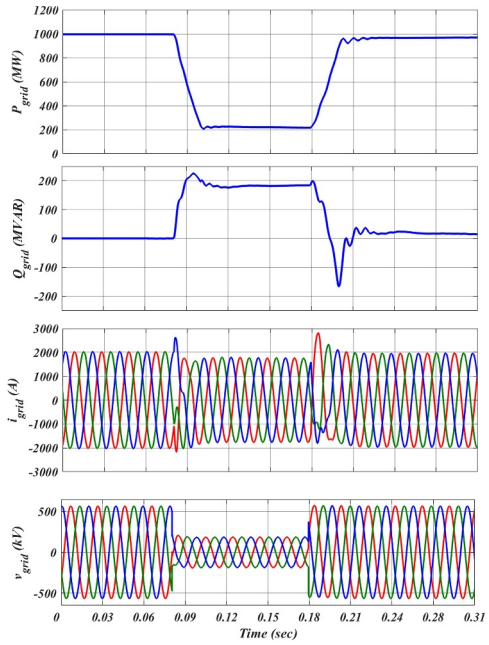

FIGURE 16 | LVRT operation of BES.

Table 4 presents a performance metrics, highlighting VSC efficiency and BES plant's current THD under varying VSC power outputs. The results show that the VSC achieves a conversion efficiency exceeding 96%, and this includes transformer losses (1%), core losses (0.1%) and copper losses (0.9%). The BES plant maintains a low-current THD, ranging from 0.24% to 0.62%. These findings demonstrate the VSC's high performance, making it well-suited for large-capacity BES applications. The performance comparison of the existing BES system [17–20] and proposed BES system is presented in Table 5.

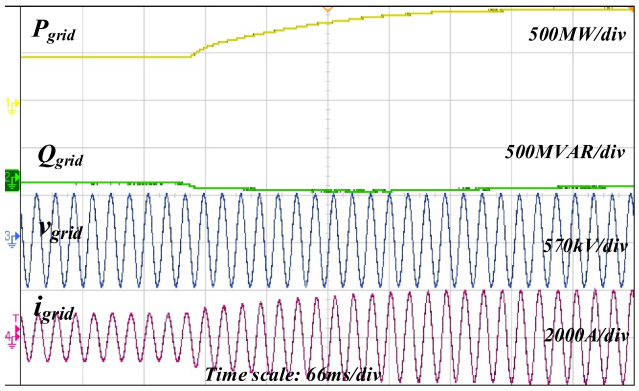

FIGURE 17 | BES plant increase in power real-time dynamic response.

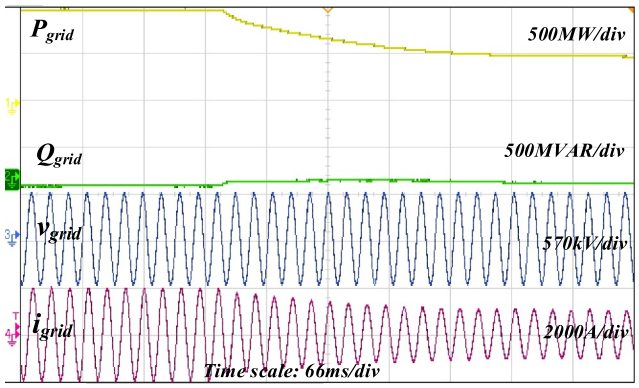

FIGURE 18 | BES plant decrease in power real-time dynamic response.

TABLE 3 | Calculation of active and reactive power during LVRT operation.

	Before LVRT	During LVRT
ΔV	0%	70%
I_S	100%	100%
I_Q	0	$0.7I_S$
I_D	I_S	$I_D = \sqrt{I_S{}^2 - I_Q{}^2}$
Apparent power ($S{=}V * I_S$)	1000 MVA	300 MVA (30% of 1000 MVA, due to the reduction of voltage to 30% of nominal value)
Reactive power (Q)	0	200 MVAR (≈70% of S, as $\Delta V = 70\%$)
Active power (P)	1000 MW	$P = \sqrt{S^2 - Q^2} = 200$MVAR

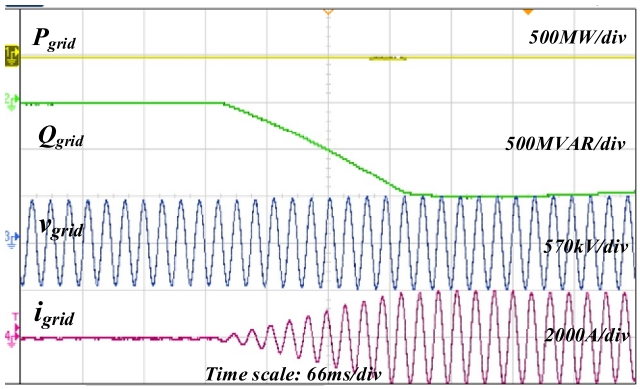

FIGURE 19 | Real-time BES plant inductive reactive power dynamic response.

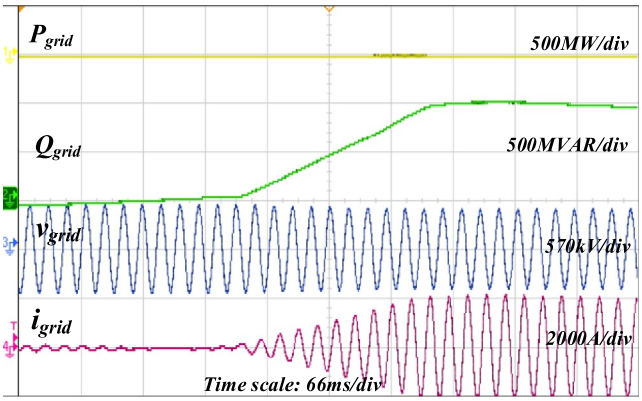

FIGURE 20 | Real-time BES plant capacitive reactive power dynamic response.

TABLE 4 | Performance matrics.

VSC power (%)	Efficiency (%)	Current THD (%)
50%	96.81	0.62
60%	96.49	0.45
70%	96.18	0.39
80%	96.08	0.30
90%	96.00	0.29
100%	96.39	0.24

4 | Conclusion

The BES plant, with capacities of 1000 MW VSC and 6000 MWh, integrates 13-level CHB converters and 30-pulse VSCs. CHB has employed a SHE modulation strategy. As a result of combining 30-pulse and SHE operation, the voltage output of VSC closely approximates a sinusoidal waveform with very low THD and a complete absence of harmonics up to 100th order. Furthermore, the output current of the BES plant demonstrates minimal THD, underscoring its capability for highly efficient energy storage and conversion operations. Performance results of BES plant are detailed, showcasing its effectiveness in both steady-state and dynamic conditions. These results demonstrate plant robust performance across various operating scenarios, whether simulated or in real-time operation.

TABLE 5 | Comparison of performance.

Attributes	Existing system [17–20]	Proposed system
BES capacity	Few MW/MWh	Multi MW/MWh
Applications	Multi	Multi
VSC topology	Two/Three level and multilevel (CHB)	Multilevel (CHB) and multipulse
VSC output voltage amplitude	Low and medium	High
Power transformer	Separate	Integrated as part of VSC
Details configuration of high-capacity BES	Not presented	Presented
Control	Mostly DQ	DQ
Response	Good	Good
VSC modulation	Mainly PWM	Fundamental
Power device switching stress and losses	High for PWM	Low
Grid integration	Mainly medium voltage level	High voltage level
Real-time implementation	Mainly simulation	Fully implemented

Acknowledgements

The authors are grateful to the ANRF Government of India for funding this work under ANRF NSC Fellowship: UKICERI: RP03391, UI-ASSIST: RP03443 and DST: RP03357 (FIST scheme).

Conflicts of Interest

The authors declare no conflicts of interest.

Data Availability Statement

Available data will be shared as per requirement.

References

1. S. Li, C. Ye, Y. Ding, Y. Song, and M. Bao, "Reliability Assessment of Renewable Power Systems Considering Thermally-Induced Incidents of Large-Scale Battery Energy Storage," *IEEE Transactions on Power Systems* 38, no. 4 (2023): 3924–3938.

2. Z. Guo, W. Wei, M. Shahidehpour, Z. Wang, and S. Mei, "Optimisationmethods for Dispatch and Control of Energy Storage With-renewable Integration," *IET Smart Grid.* 5, no. 3 (2022): 137–160, https://doi.org/10.1049/stg2.12063.

3. M. M. Elsaied, W. H. AbdelHameed, and H. M. Hasanien, "Frequency Stabilizationof a Hybrid Three-Area Power System Equipped

Withenergy Storage Units and Renewable Energy Sources," *IET Renewable Power Generation* 16, no. 15 (2022): 3267–3286, https://doi.org/10.1049/rpg2.12577.

4. S. Suthar and N. M. Pindoriya, "Energy Management Platform for Integrated Battery-Based Energy Storage – Solar PV System: A Case Study," *IET Energy Syst. Integr.* 2, no. 4 (2024): 373–381, https://doi.org/10.1049/iet-esi.2020.0035.

5. S. Karmakar, B. Singh, A. Chandra, and K. Al-Haddad, "Thirteen-Level Cascaded H-Bridge Converters and 30-Pulse Converter Transformer Based High-Power Voltage Source Converters for Large-Scale Integration of Battery Energy Storage," in *IEEE 14th International Conference on Power Electronics and Drive Systems (PEDS)* (2023), 1–6.

6. A. Bera, B. R. Chalamala, R. H. Byrne, and J. Mitra, "Sizing of Energy Storage for Grid Inertial Support in Presence of Renewable Energy," *IEEE Trans.Power Systems* 37, no. 5 (2022): 3769–3778, https://doi.org/10.1109/tpwrs.2021.3134631.

7. G. Scaglione, C. Nevoloso, G. A. Schettino, O. D. Tommaso, and R. Miceli, "A Novel Multiobjective Finite Control Set Model Predictive Control for IPMSM Drive Fed by a Five-Level Cascaded H-Bridge Inverter," *IEEE Journal of Emerging and Selected Topics in Power Electronics* 12, no. 2 (2024): 1959–1973, https://doi.org/10.1109/jestpe.2024.3362404.

8. X. Wang, Y. Zhao, R. Yang, W. Hu, and T. Zou, "Model Predictive-Based Fault-Tolerant and Power Balancing Control for Cascaded H-Bridge Inverter," *IEEE Transactions on Power Electronics* 39, no. 5 (2024): 5257–5270, https://doi.org/10.1109/tpel.2023.3349311.

9. A. Mohammadhassani and A. Mehrizi-Sani, "Fast and Fault-Tolerant modelpredictive Control of MMCs Under Selective Harmonicelimination," *IET Generation, Transmission & Distribution* 17 (2023): 240–251.

10. P. Kala, V. Jately, A. Sharma, et al., "GWO-NR Hybrid Method for Selective Harmonic Elimination in Multilevel Inverter for Distributed Energy Systems," *IEEE Access* 12 (2024): 27957–27972, https://doi.org/10.1109/access.2024.3366549.

11. S. Pan, M. Wu, J. Wang, et al., "Unified Switching Frequency Minimized Harmonic Mitigation Technique for Asymmetric Cascaded H-Bridge Converters," *IEEE Journal of Emerging and Selected Topics in Power Elect.* 12, no. 2 (2024): 2006–2016, https://doi.org/10.1109/jestpe.2024.3364246.

12. R. Abdollahi and G. B. Gharehpetian, "Suggestion of DC Side Passive Harmonic Reductioncircuits for Industrial Applications Based on Acomparative Study," *IET Power Electronics* 15, no. 6 (2022): 531–547, https://doi.org/10.1049/pel2.12247.

13. Y. Lian, S. Yang, X. Zeng, H. Ben, and W. Yang, "Comparative Analysis of Two Different Interphase Reactors Applied in 36-Pulse Diode Rectifier," *IET Electric Power Applications* 14, no. 6 (2020): 1011–1022, https://doi.org/10.1049/iet-epa.2019.0671.

14. Q. Li, F. Meng, L. Gao, H. Zhang, and Q. Du, "A 30-Pulse Rectifier Using Passive Voltage Harmonic Injection Method at DC Link," *IEEE Transactions on Industrial Electronics* 67, no. 11 (2020): 9273–9291, https://doi.org/10.1109/tie.2019.2956404.

15. J. Wang, T. Liu, T. Yu, C. Zhao, X. Yao, and Q. Chen, "A Series-Connected 24-Pulse Star Rectifier Employing Two Different Pulse-Doubling Interphase Reactors," *IEEE Transactions on Power Electronics* 39, no. 1 (2024): 1460–1481, https://doi.org/10.1109/tpel.2023.3323795.

16. X. Zhang, Y. Li, J. Li, T. Wu, S. Yang, and Z. Hao, "DC-Sidestability Analysis of Grid-tied Converter With Differentcontrol Modes Based on Electrical Torque Analysis," *IETEnergy Syst. Integr.* 6, no. 1 (2024): 31–44, https://doi.org/10.1049/esi2.12110.

17. M. R. Jannesar, S. Sadr, and M. Savaghebi, "Optimal Sitting, Sizing and Control of Battery Energy Storage to Enhance Dynamic Stability of Low-Inertia Grids," *IET Renewable Power Generation* 18, no. 15 (2024): 2925–2941, https://doi.org/10.1049/rpg2.13079.

18. B. Li, P. Chen, G. Li, et al., "Fault Diagnosis Technology Overview for Lithium-ion Battery Energy Storage Station," *IET Energy Syst. Integr.* 1–18 (2024).

19. M. Liu, C. Cao, P. Wang, et al., "A Review of Power Conversion Systems and Design Schemes of High-Capacity Battery Energy Storage Systems," *IEEE Access* 10 (2022): 52030–52042, https://doi.org/10.1109/access.2022.3174193.

20. J. Li, Z. Fang, Q. Wang, M. Zhang, Y. Li, and W. Zhang, "Optimal Operation With Dynamic Partitioning Strategy for Centralized Shared Energy Storage Station With Integration of Large-Scale Renewable Energy," *Journal of Modern Power Systems and Clean Energy* 12, no. 2 (2024): 359–370, https://doi.org/10.35833/mpce.2023.000345.

Appendix A

The BES plant operates at 400 kV and 50 Hz. It includes a three-winding tie transformer rated at 400 kV/132 kV and 500 MVA. There are 20 VSCs, each with a capacity of 50 MW. The BES plant is rated at 1000 MW with a 6000-MWh energy storage capacity. The key specifications of the BES plant is presented in Table A1.

TABLE A1 | Key specifications.

Attributes	Parameters
BES plant capacity	1000 MW and 6000 MWh
BES plant grid voltage	400 kV
VSC capacity	50 MW
VSC numbers	20
VSC generated voltage	132 kV
CHB numbers per VSC	5
CHB level	13-level with total 18 numbers of H-bridge
Device count per H-bridge	2 × 4 (600V IGBT) = 8
H-bridge battery DC voltage	1644 V (rated), 1344–1881 V (operating range)
H-bridge battery current rating	400 A for 6 h